Highly linear heterogeneous-integrated Mach-Zehnder interferometer modulators on Si

CHONG ZHANG,[1,*] PAUL A. MORTON,[2] JACOB B. KHURGIN,[3] JON D. PETERS,[1] AND JOHN E. BOWERS[1]

[1]*Department of Electrical and Computer Engineering, University of California, Santa Barbara, CA 93106, USA*
[2]*Morton Photonics, West Friendship, MD, USA*
[3]*Department of Electrical and Computer Engineering, Johns Hopkins University, Baltimore, MD, USA*
[*]*czhang@ece.ucsb.edu*

Abstract: In this paper we demonstrate highly linear Mach-Zehnder interferometer modulators utilizing heterogeneous integration on a Si substrate (HS-MZM). A record high dynamic range was achieved for silicon devices, obtained using hybrid III-V/Si phase modulation sections and single drive push-pull operation, demonstrating a spurious free dynamic range (SFDR) of 112 dB·Hz$^{2/3}$ at 10 GHz, comparable to commercial Lithium Niobate MZMs.

References and links

1. G. C. Valley, "Photonic analog-to-digital converters," Opt. Express **15**(5), 1955–1982 (2007).
2. W. S. C. Chang, *RF Photonic Technology in Optical Fiber Links* (Cambridge University Press, 2002), Chap. 4.
3. R. G. Walker, N. I. Cameron, Y. Zhou, and S. J. Clements, "Optimized gallium arsenide modulators for advanced modulation formats," IEEE J. Sel. Top. Quantum Electron. **19**(6), 3400912 (2013).
4. J. Yu, C. Rolland, D. Yevick, A. Somani, and S. Bradshaw, "A novel method for improving the performance of InP/InGaAsP multiple-quantum-well Mach-Zehnder modulators by phase shift engineering," in *Proc. IPR′ 96* (1996), paper 1TuG4–1.
5. W. Forysiak and D. S. Govan, "Progress towards 100-G digital coherent pluggables using InP-based photonics," J. Lightwave Technol. **32**(16), 2925–2934 (2014).
6. P. Dong, L. Chen, and Y. K. Chen, "High-speed low-voltage single-drive push-pull silicon Mach-Zehnder modulators," Opt. Express **20**(6), 6163–6169 (2012).
7. H. Yi, Q. Long, W. Tan, L. Li, X. Wang, and Z. Zhou, "Demonstration of low power penalty of silicon Mach-Zehnder modulator in long-haul transmission," Opt. Express **20**(25), 27562–27568 (2012).
8. L. Liao, A. Liu, D. Rubin, J. Basak, Y. Chetrit, H. Nguyen, R. Cohen, N. Izhaky, and M. Paniccia, "40 Gbit/s silicon optical modulator for high speed applications," Electron. Lett. **43**(22), 1196–1197 (2007).
9. C. H. Cox III, E. I. Ackerman, G. E. Betts, and J. L. Prince, "Limits on the performance of RF-over-fiber links and their impact on device design," IEEE Trans. Microw. Theory Tech. **54**(2), 906–920 (2006).
10. M. Streshinsky, A. Ayazi, Z. Xuan, A. E.-J. Lim, G.-Q. Lo, T. Baehr-Jones, and M. Hochberg, "Highly linear silicon traveling wave Mach-Zehnder carrier depletion modulator based on differential drive," Opt. Express **21**(3), 3818–3825 (2013).
11. X. Xie, J. B. Khurgin, J. Kang, and F-S. Chow, "Linearized Mach-Zehnder intensity modulator," IEEE PTL, **15**, 531–533 (2003).
12. J. Cardenas, P. A. Morton, J. B. Khurgin, A. Griffith, C. B. Poitras, K. Preston, and M. Lipson, "Linearized silicon modulator based on a ring assisted Mach Zehnder inteferometer," Opt. Express **21**(19), 22549–22557 (2013).
13. T. Komljenovic, M. Davenport, J. Hulme, A. Liu, C. Santis, A. Spott, S. Srinivasan, and C. Eric Stanton, "Zhang, J. E. Bowers, "Heterogeneous silicon photonic integrated circuits," J. Lightwave Technol. **34**(1), 20–35 (2016).
14. H.-W. Chen, "High-Speed Hybrid Silicon Mach-Zehnder Modulator and Tunable Microwave Filter," PhD thesis, University of California Santa Barbara, 2011.
15. M. Usman Sadiq, J. O'Callaghan, B. Roycroft, K. Thomas, E. Pelucchi, F. H. Peters, and B. Corbett, "Study of electro-optic effect in asymmetrically ramped AlInGaAs multiple quantum well structures," Phys. Status Solidi., A Appl. Mater. Sci. **213**(4), 930–935 (2016).
16. D. Liang, A. W. Fang, H. Park, T. E. Reynolds, K. Warner, D. C. Oakley, and J. E. Bowers, "Low-temperature, strong SiO2-SiO2 covalent wafer bonding for III–V compound semiconductors-to-silicon photonic integrated circuits," J. Electron. Mater. **37**(10), 1552–1559 (2008).
17. V. R. Almeida, R. R. Panepucci, and M. Lipson, "Nanotaper for compact mode conversion," Opt. Lett. **28**(15), 1302–1304 (2003).

18. C. Xiong, D. Gill, J. Rosenberg, M. Khater, T. Barwicz, S. Assefa, S. Shank, C. Reinholm, E. Kiewra, J. Ellis-Monaghan, S. Kamlapurkar, A. Stricker, W. Green, Y. A. Vlasov, and W. Haensch, "A linear push-pull silicon optical modulator," in *FiO/LS* (2014), paper FM3A.4.
19. Y. Zhou, L. Zhou, F. Su, J. Xie, H. Zhu, X. Li, and J. Chen, "Linearity measurement of a silicon single-drive push-pull Mach-Zehnder modulator," CLEO, 2015.
20. A. Ayazi, T. Baehr-Jones, Y. Liu, A. E. Lim, and M. Hochberg, "Linearity of silicon ring modulators for analog optical links," Opt. Express **20**(12), 13115–13122 (2012).
21. A. M. Gutiérrez, J. V. Galan, J. Herrera, A. Brimont, J. Martí, D. Marris-Morini, L. Vivien, J.-M. Fédéli, D. J. Thomson, F. Y. Gardes, G. T. Reed, and P. Sanchis, "Silicon-based electro-optic modulators for linear and nonlinear radio-over-fiber applications," in *2012 International Topical Meeting on Microwave Photonics* (2012), 168–171.
22. A. M. Gutiérrez, J. V. Galan, J. Herrera, A. Brimont, D. Marris-Morini, J.-M. Fédéli, L. Vivien, and P. Sanchis, "High linear ring-assisted MZI electro-optic silicon modulators suitable for radio-over-fiber applications," in *The 9th International Conference on Group IV Photonics* (2012), paper 57–59.
23. L. Chen, J. Chen, J. Nagy, and R. M. Reano, "Highly linear ring modulator from hybrid silicon and lithium niobate," Opt. Express **23**(10), 13255–13264 (2015).

1. Introduction

The non-linearity of an electro-optic modulator causes signal distortion, reducing its dynamic range, therefore limiting its application in analog radio frequency (RF) photonics systems. Commercial Lithium Niobate ($LiNbO_3$) Mach-Zehnder interferometer modulator (MZM) devices are widely used in such systems [1, 2], however, these devices are bulky and expensive, limiting addressable applications. Semiconductor based devices offer the chance to obtain highly linear performance together with small size, low cost, and the ability to integrate them with additional components to form photonic integrated circuit (PIC) devices. High performance MZMs have been developed based on GaAs [3] and InP [4], with the InP devices offering the opportunity to combine the MZM with other components (e.g. laser, photodetector) to develop photonics integrated circuits [5] for commonly used telecom bands.

The silicon photonics platform takes advantage of the tremendous investment and expertise in designing and fabricating devices on large Si wafers using standard CMOS foundry processes; enabling large scale integration with high repeatability, plus high volume manufacturing with low cost. An MZM fabricated on a silicon photonics platform is therefore of great interest [6, 7]. Silicon MZMs, while significantly smaller than $LiNbO_3$ MZMs, are still relatively long for a semiconductor modulator due to low phase modulation efficiency [8], requiring either longer MZM lengths or higher modulation voltages. Additionally, and more importantly for analog systems, the nonlinearity of a Si MZM is significantly increased compared to a $LiNbO_3$ MZM, due to the inherent nonlinearity of the Si phase modulation mechanism based on free carrier insertion or depletion. While a typical optical link using a $LiNbO_3$ MZM may have a spurious free dynamic range (SFDR) of up to 113 dB·$Hz^{2/3}$ [9], much lower values have been found with Si MZM devices. Some improvement in the linearity of Si MZMs was achieved by using differential drive to reduce the non-linearity of the Si PN junction phase section, providing an SFDR of up to 97 dB·$Hz^{2/3}$ at 1 GHz modulation frequency [10]. Record high SFDR of 106 dB·$Hz^{2/3}$ at 1 GHz, and 99 dB·$Hz^{2/3}$ at 10 GHz was obtained for Si based modulators using a Ring Assisted Mach-Zehnder Interferometer (RAMZI) modulator structure [11, 12]. In these devices the inherent nonlinearity of the Mach-Zehnder Interferometer (MZI) plus the nonlinearity of the silicon phase modulators is mitigated by the opposite sign of nonlinearity created in the highly coupled ring phase modulators. While the RAMZI modulator devices improved upon the performance of Si MZMs, and further improvement is expected if the nonlinearity cancellation is optimized, neither of these results approaches the performance of commercial $LiNbO_3$ MZMs.

In this work, the linearity performance of silicon photonics based MZMs using heterogeneously integrated phase modulation sections fabricated from hybrid III-V multiple quantum-well (MQW)/Si waveguides was investigated. The heterogeneous Si integration platform adopts a CMOS compatible process, with advantages in the flexibility of integrating different material systems on silicon-on-insulator (SOI) [13]. The use of hybrid III-V/Si phase modulation sections was chosen due to the lower nonlinearity of the III-V MQWs, together

with the potential for higher optical power level operation, compared to Si based devices. The design, fabrication and testing of these HS-MZM devices, is described in the following sections.

2. Device design and fabrication

Unlike Si, the heterogeneously integrated III-V materials are not centro-symmetric and have a direct bandgap, therefore, in addition to the plasma and Kerr effects present in Si, they also exhibit a strong Pockels effect and quantum confined Stark effect (QCSE) [14, 15]. This provides extra degrees of freedom to achieve high linearity MZMs, and also helps to increase the modulation efficiency (lower V_π) plus provides for devices with larger bandwidth and a compact footprint.

The refractive index in the heterogeneous waveguide changes as a function of the applied voltage as:

$$\Delta n(\lambda, f) = \sum_{m=1}^{4} \sum_{k=1}^{4} c_{mk}(\lambda) V^k \tag{1}$$

where m = 1:4 refers to the mechanism of the index change, respectively plasma effect, band filling, QCSE and Pockels effect [14] and order k is truncated at 4 because it is the fourth order term that is responsible for the third order distortion. The applied voltage consists of bias V_b and signal $V_s(t)$, hence the index change can be expanded near the bias point as:

$$\Delta n(\lambda, f) = \sum_{m=1}^{4} \sum_{k=1}^{3} \left[c_{mk} + (k+1)c_{m,k+1}V_b + ... \right] V_s^k(t) \tag{2}$$

The response of the MZI modulator biased at quadrature and operating in push-pull mode can be then written as,

$$P_s \sim \sin\left(\frac{2\pi \Delta n L}{\lambda} \right) \approx \frac{2\pi \Delta n L}{\lambda} - \frac{1}{6}\left(\frac{2\pi \Delta n L}{\lambda} \right)^3 \tag{3}$$

and substitution yields the third order distortion as,

$$P_s^{(3)} = \sum_{m=1}^{4} \left[\frac{2\pi L}{\lambda}\left(c_{m3} + 4c_{m4}V_b \right)^3 \right] V_s^3(t) - \frac{1}{6}\left[\frac{2\pi L}{\lambda} \sum_{m=1}^{4}\left(c_{m1} + 2c_{m2}V_b + 3c_{m3}V_b^2 + 4c_{m4}V_b^3 \right) \right]^3 V_s^3(t) \tag{4}$$

The coefficients c_{13}, c_{14} (plasma) and c_{23}, c_{24} (band filling) are negative, while the coefficients c_{33}, c_{34} (QCSE) are positive and also large in absolute value [14]. In other words, the QCSE does not saturate with applied voltage, at least for reasonably small voltages. For the Pockels effect only the linear term c_{41} is non-zero. Since (with exception of the Pockels effect) coefficients are wavelength dependent, especially those associated with the QCSE, at one particular wavelength the positive third order distortion of the QCSE will compensate the negative distortions of band filling, plasma and the MZI itself.

The HS-MZM structures and the CMOS compatible process flow used to fabricate the devices are shown schematically in Fig. 1. The devices are an MZI with balanced arms which include the hybrid III-V/Si phase modulators with tunable Directional Coupler (DC) or Multimode Interference (MMI) devices as the 3-dB power splitter and combiners forming the MZI. NiCr heaters were used to tune the DC devices for 50/50 splitting, and were also used within the arms of the MZI to thermally tune its operating point.

Fabrication was carried out using an SOI substrate with a 500 nm Si device layer and a 1 μm buried oxide layer. An ASML PAS 5500/300 DUV stepper with 248 nm light source and 150 nm minimum feature size was used. This enables a higher optical mode confinement factor in the MQWs from a narrower width waveguide. Careful calibration was performed to tune the dimension of the passive components such as directional couplers. The Si waveguide was etched with SF_6/C_4F_8 plasma, providing a propagation loss of 1.6 ± 0.3 dB/cm for the 600

nm waveguide width (Fig. 1(a)). Diced III-V epi was then transferred to the patterned SOI substrate with a low temperature molecular bonding technique (Fig. 1(b)) [16]. A reactive ion etch tool was utilized to etch the III/V p-mesa and stop in the InAlGaAs active region, which was cleared afterwards with a selective wet etch to expose the bottom n-type contact layer. Pd/Ti/Pd/Au and Pd/Ge/Pd/Au stacks were deposited for p-type and n-type ohmic contacts, respectively (Fig. 1(c)). A 1 μm SiO$_2$ insulation layer was deposited, then NiCr heaters were deposited on top of that layer. Large gold metal pads were deposited after through-via etches in the thick insulation layer (Fig. 1(d)).
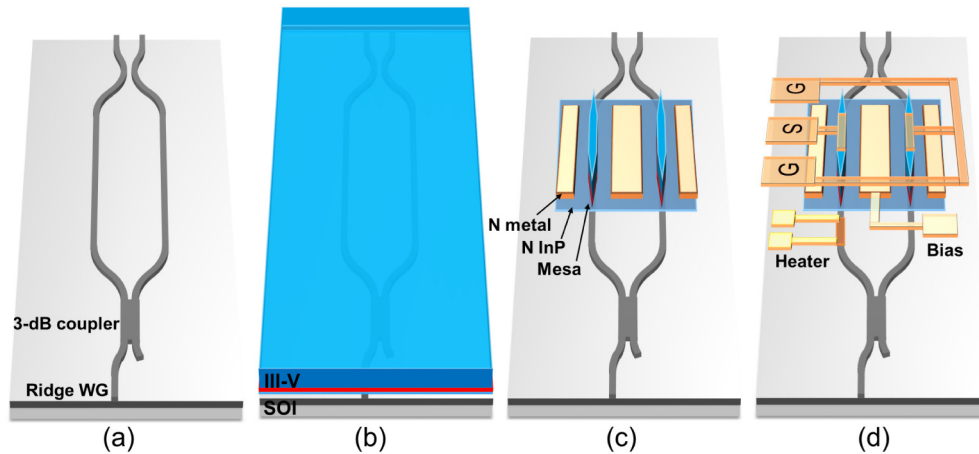
Fig. 1. Process flow of the HS-MZM: (a) Si WG etch; (b) materials bonding; (c) III-V etch and n-contact; (d) Metallization.

The bonded III-V materials stack includes an active region with 15 InAlGaAs QWs with a photoluminescence (PL) wavelength centered at 1360 nm; the details shown in Table 1. The QWs were slightly n-doped to improve the high speed performance [14]. Separate confinement heterostructure (SCH) layers were designed properly to improve the optical mode confinement in the QWs. The doping level in the p-InGaAs layer was raised by 50% compared with a previously used design [14], to lower the p-contact resistance, which normally dominates the series resistance of devices with a narrow p-mesa. In order to optimize the modulator efficiency, the III-V phase modulation sections were aligned parallel to the [011] crystalline orientation, so that the Pockels effect adds constructively to the other index changes. A high transverse electric (TE) optical mode confinement of 26.9% in the MQWs was achieved with a 600 nm wide Si WG and a 2.5 μm mesa, as shown in the cross sectional plot in Fig. 2(a). Figures 2(b) and 2(c) shows SEM images of the III-V mesa with a 50 μm long taper between this hybrid section and the Si waveguide. The taper tip width is smaller than 200 nm, providing low coupling loss between the Si waveguide and the hybrid section.

Table 1. The epitaxial III-V layers

| Layer composition	Doping level	Thickness (nm)
P-type contact In$_{0.53}$Ga$_{0.47}$As	Zn: 1.5×10^{19}	100
Band smooth layer	Zn: 3×10^{18}	50
P-type cladding InP	Zn: 1.5×10^{18} -> 5×10^{17}	1500
SCH InGaAsP 1.25Q	Si: 1×10^{17}	100
15 × QW In$_{0.574}$Al$_{0.111}$Ga$_{0.315}$As	Si: 1×10^{17}	8
16 × Barrier In$_{0.468}$Al$_{0.217}$Ga$_{0.315}$As		5
SCH InGaAsP 1.25Q	Si: 3×10^{18}	50
N-type contact InP	Si: 3×10^{18}	110
Bonding layer with supper lattices	Si: 3×10^{18}	40
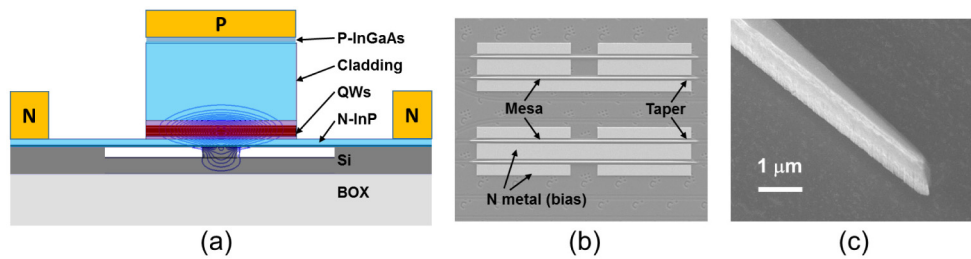
Fig. 2. (a) The cross-section of the devices with intensity contour of fundamental TE mode; (b) top view SEM image of HS-MZM; (c) SEM image of taper tip from angled view.

3. Device characterization

The processed chips with polished facets were placed on a thermal heat sink which was temperature controlled at 25°C for testing. A single drive push-pull electrical configuration was utilized in the devices for ease of modulation [6], requiring only one RF drive signal, and to take advantage of the reduced capacitance of that approach. A tunable laser source with TE polarization and polarization maintaining (PM) fiber output was coupled into the Si waveguide using a PM lensed fiber. The output of the HS-MZM was coupled into a fiber using a fiber lens, and for SFDR measurements was amplified by an Er-Doped Fiber Amplifier (EDFA) and coupled into a photo detector (PD). Two HS-MZM devices are shown in Fig. 3: the left one uses an MMI coupler as the 3 dB power splitter in the MZI; the right one, which is fiber coupled in the image, uses a tunable directional coupler that can be tuned to a 3 dB split ratio according to the input wavelength. The input and output waveguides were angled to reduce optical reflections; however, the tapered design produces relatively high coupling loss (8 to 10 dB per facet) although with relatively easy alignment. Future devices will incorporate an inverse taper design [17] in order to provide much lower coupling loss, as required for a discrete modulator device.
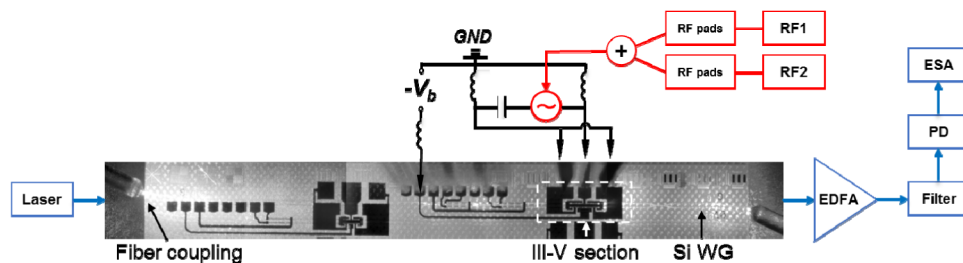

Fig. 3. NIR image of an MZM device, and setup for SFDR measurement.

DC measurements were taken under computer control to characterize single drive push-pull operation of the devices at multiple wavelengths. Figure 4 shows measurements of the output versus the differential voltage between the two phase modulation sections, for a device with a short (100 μm) phase modulation section length, and for different input optical wavelengths of 1550 nm, 1500 nm and 1460 nm. Much higher modulation efficiency (lower V_π) is seen at the shorter wavelength, closer to the band-edge off the phase modulator epi material. The device is biased near quadrature for all of the transfer characteristics shown in Fig. 4. The $V_\pi \cdot L$ of the device can be fit from this measured data, which is a minimum of 1.5 V·mm at 1460 nm, and larger at longer wavelength. The actual V_π is higher in this particular device due to its short length. The larger V_π compared with previous results on similar hybrid silicon MZI modulators [14], probably results from a reduction of mode confinement in the MQWs of a narrower III/V mesa, from undercut of the MQWs layers in the wet-etch step, or the voltage drop on a higher series resistance due to the narrower mesa.
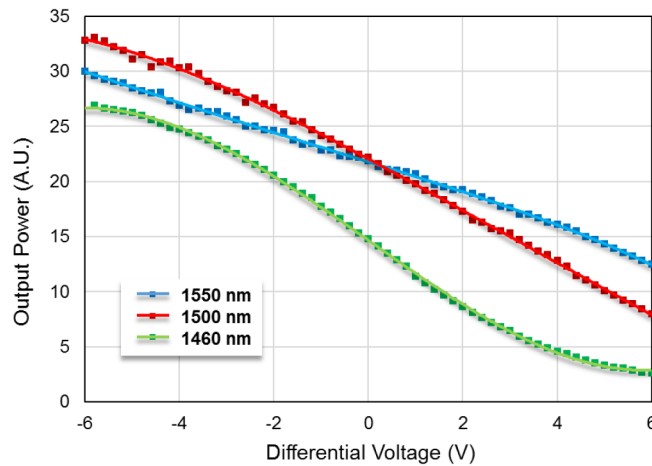
Fig. 4. Transmission measurement of 100 μm HS-MZM at multiple wavelengths.

The apparent linearity of the DC characteristics may change with wavelength, indicating a delicate interplay of the different phase modulation mechanisms described above, however, this is difficult to quantify from DC measurements alone. The third order nonlinearity, i.e. the third order term in the series expansion, of the sinusoidal-like response of the MZI is negative. Also negative are the third order terms in the series expansion of the plasma-like effect of free carriers and the state-blocking phase change effect. At the same time, the phase characteristics of the QCSE have a positive third order term, and also a strong wavelength dependence. The fourth phase modulation mechanism, the Pockels effect, is largely linear. As a result, at some wavelength and modulator bias the positive nonlinearity of the QCSE phase response could become sufficient to cancel the negative nonlinearities of the plasma and state blocking effects, and potentially also the nonlinearity of the MZI itself. By choosing the optimum bias point this high linearity wavelength can be shifted towards the desired value of 1550nm, however, complete optimization, and therefore linearization of the response, may require an MQW design with a longer PL wavelength than used in these devices.
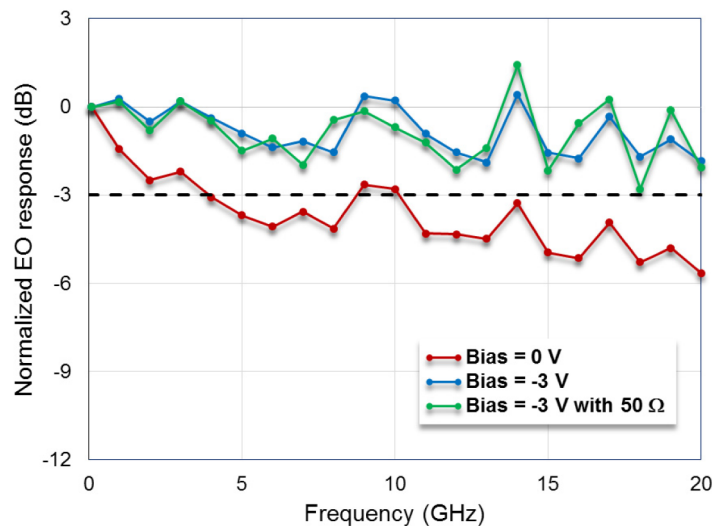

Fig. 5. Measured Frequency Response for 100 μm HS-MZM: unterminated, 0V, −3V; 50 Ohm −3V.

Frequency response measurements of the 100 μm device, demonstrating a bandwidth of over 20 GHz, are shown in Fig. 5. Terminating the device with a 50 Ohm load shows little improvement in device bandwidth (up to 20 GHz), while reducing the efficiency by 3 dB compared to no matching load. Biasing the device at 0 V shows an increase in low frequency response, likely due to the small swing to positive bias from the sinusoidal input.
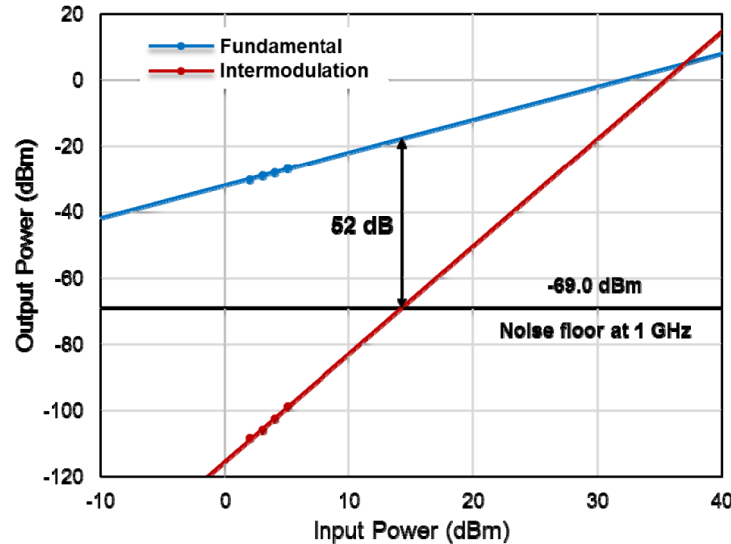

Fig. 6. Measured SFDR for 100 μm device. 52 dB for 1 GHz Bandwidth, or 112 dB·Hz$^{2/3}$.

To assess linearity, measurements of the SFDR of this same device were carried out at a wavelength of 1550 nm, and a modulation frequency of 10 GHz. An EDFA was used to overcome the loss of the two fiber couplings (16 to 20 dB), plus provide sufficient optical power at the PD to support high SFDR operation. The requirement to use an EDFA limited the wavelength range over which SFDR could be measured, limiting the possibility to further improve the performance by increasing the QCSE. As shown in Fig. 3, two RF tones were combined using a power combiner and RF pads and applied to the device. The separation between two tones was set to 10 MHz, so the two signals were at 9995 MHz and 10005 MHz for the 10 GHz center frequency. The generated third order intermodulation distortion signals were at 9985 MHz and 10015 MHz, respectively. The fundamental and third order intermodulation products were measured on a high performance electrical spectrum analyzer.

The SFDR was measured versus variations in the input optical power level to the MZM, versus modulator p-n junction dc bias voltage, and for different photodetector currents. A series of SFDR traces were taken, with the highest SFDR occurring for the highest optical input power level (+ 18 dBm laser output) and also highest photocurrent (15.6 mA), for a DC bias voltage of −2 V. The measured response in Fig. 6 shows the highest SFDR; in this case the plot has an SFDR of 52 dB for 1 GHz bandwidth, or an SFDR of 112 dB·Hz$^{2/3}$.

Figure 7 compares major results of recent works on the linearity of modulators fabricated on a Si, CMOS compatible platform [10, 12, 18–23]. This work surpasses the previous record for a linearized modulator on Si, obtained using the RAMZI modulator design [12], without the need of coupled microresonators and their wavelength dependent operation. It is significantly higher than any Si MZM result. This result demonstrates that heterogeneously integrated III-V/Si modulators, using wafer bonded III-V material for phase modulation sections, can produce performance similar to Lithium Niobate devices [9], eliminating the nonlinearity added by using Si phase modulators, and provides a promising solution for highly integrated RF photonics applications.
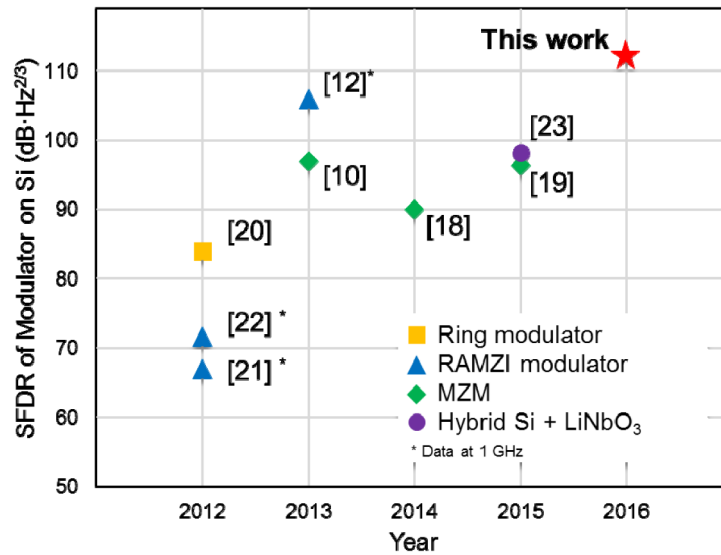
Fig. 7. Comparison of modulators on Si: SFDR representing the degree of linearity.

4. Conclusions

In this work we have demonstrated that high SFDR of up to 112 dB·Hz$^{2/3}$ at a 10 GHz modulation frequency can be achieved in a heterogeneously integrated III-V on Si MZM, a value similar to that achieved using commercial LiNbO$_3$ MZMs. The high SFDR is achieved through the use of low nonlinearity III-V MQW phase modulation sections, the device biased to minimize nonlinear effects, leaving only the nonlinearity of the MZI itself. Further optimization offers the opportunity to linearize the MZI response itself, by increasing the QCSE in the phase modulation sections. This result enables the development of high performance RF photonics systems on a CMOS compatible platform that includes heterogeneous integration of III-V materials.

Acknowledgment